Correspondence to:
D. S. Ozturk,
dogacan.s.ozturk@jpl.nasa.gov

Response of the Geospace System to the Solar Wind Dynamic Pressure Decrease on 11 June 2017: Numerical Models and Observations

Dogacan S. Ozturk[1] [ID], **Shasha Zou[2]** [ID], **James A. Slavin[2]** [ID], and **Aaron J. Ridley[2]** [ID]

[1]Jet Propulsion Laboratory, California Institute of Technology, Pasadena, CA, USA, [2]Department of Climate and Space Sciences and Engineering, University of Michigan, Ann Arbor, MI, USA

Abstract   On 11 June 2017, a sudden solar wind dynamic pressure decrease occurred at 1437 UT according to the OMNI solar wind data. The solar wind velocity did not change significantly, while the density dropped from 42 to 10 cm^{-3} in a minute. The interplanetary magnetic field B_Z was weakly northward during the event, while the B_Y changed from positive to negative. Using the University of Michigan Block Adaptive Tree Solarwind Roe Upwind Scheme global magnetohydrodynamic code, the global responses to the decrease in the solar wind dynamic pressure were studied. The simulation revealed that the magnetospheric expansion consisted of two phases similar to the responses during magnetospheric compression, namely, a negative preliminary impulse and a negative main impulse phase. The simulated plasma flow and magnetic fields reasonably reproduced the Time History of Events and Macroscale Interactions during Substorms and Magnetospheric Multiscale spacecraft in situ observations. Two separate pairs of dawn-dusk vortices formed during the expansion of the magnetosphere, leading to two separate pairs of field-aligned current cells. The effects of the flow and auroral precipitation on the ionosphere-thermosphere (I-T) system were investigated using the Global Ionosphere Thermosphere Model driven by simulated ionospheric electrodynamics. The perturbations in the convection electric fields caused enhancements in the ion and electron temperatures. This study shows that, like the well-studied sudden solar wind pressure increases, sudden pressure decreases can have large impacts in the coupled I-T system. In addition, the responses of the I-T system depend on the initial convection flows and field-aligned current profiles before the solar wind pressure perturbations.

1. Introduction

Sudden variations in the solar wind dynamic pressure cause global changes in the magnetospheric configuration, disrupt the magnetospheric and ionospheric current systems, and result in large-scale flow perturbations (Fujita et al., 2003a, 2003b; Kivelson & Southwood, 1991; Samsonov & Sibeck, 2013; Yu. & Ridley, 2011). The response of the geospace system to the sudden enhancements of the solar wind dynamic pressure, known as sudden storm commencements or sudden impulses (SIs; Araki, 1994a) has been traditionally studied using ground magnetometer observations. These ground magnetometer observations show temporal, latitudinal, and longitudinal dependencies (Araki, 1994a, 1994b; Sun et al., 2014) indicating that they may be due to the different magnetospheric and ionospheric sources (Fujita et al., 2003a, 2003b; Kivelson & Southwood, 1991). The high-latitude magnetometer observations of SIs show that the compression signature can be decomposed as a short-lived preliminary impulse (PI) and a succeeding longer-lived main impulse (MI; Araki, 1994a, 1994b). The combination of these impulse signatures creates a bipolar response, with its polarity dependent on the magnetic local time (MLT) and magnetic latitude. Investigating the physical processes being dependent on the formation and propagation of the SI signatures is an important aspect of understanding solar wind-magnetosphere interaction.

Apart from the SI events related to the solar wind dynamic pressure enhancements, which will be referred to as SI^+ from here on, the solar wind dynamic pressure decreases can also cause global disruptions in the geospace system. Araki and Nagano (1988) showed that high-latitude ground magnetometers observed bipolar responses with opposite polarities to those of SI^+s, during sudden expansions of the magnetosphere after the solar wind dynamic pressure dropped. In addition, they used geosynchronous spacecraft measurements to show that the magnetic field parallel to Earth's rotation axis decreased as a result of expansion. Ground

magnetometer observations at lower latitudes showed that this decrease was preceded by a short-lived initial positive perturbation. Except this initial positive perturbation at the low latitudes, they concluded that SI^-s can be explained by the "mirror image" of the same model derived for SI^+s (Araki, 1994a). Only five events were investigated in this early study, and more events are needed to conclusively determine whether the SI^- events are mirror images of the SI^+ events.

To explain the distribution and the polarization of the SI^-s further, Takeuchi et al. (2000) conducted a study using higher temporal resolution ground magnetometer data and further distinguished the SI^- signatures from that of an opposite SI^+ at certain locations on the ground. They investigated the SI^- response with a larger data set consisting of 28 events (Takeuchi et al., 2002) and confirmed that the SI^- generation can be explained by simply reversing the direction of the electric field in the equatorial plane that occurs due to the sunward motion of the magnetopause. They suggested that magnetospheric compression and expansion mechanisms lead to oppositely rotating ionospheric vortices. They concluded that similarities arise between SI^+ and SI^- signals based on the relative location of the ground magnetometers to the overhead vortices.

As opposed to the SI^+s, there is no strong link between geomagnetic storms and SI^-s since they are usually associated with reverse shocks, but studies have been carried out investigating the relationship between SI^-s and geomagnetic activity. Sato et al. (2001) was the first one to show that the optical aurora can be enhanced due to solar wind dynamic pressure drops. They investigated a sharp dynamic pressure decrease from 12 to 2 nPa and used DMSP satellite measurements to show enhanced electron precipitation and an associated upward field-aligned current (FAC) system at dusk. They argued that field line resonance might be the reason for the acceleration of electrons, as opposed to loss cone instability which is responsible for the enhanced optical emissions during SI^+s (Zhou & Tsuratani, 1999). Liou (2007) further investigated the link between SI^-s and geomagnetic activity with a data set of 13 large solar wind dynamic pressure drop events. Using the ultraviolet imager on the Polar satellite and ground magnetometer observations, they found that 3 of the 13 events were associated with substorms, and an increase in the open flux was necessary to trigger a substorm regardless of the magnitude of the dynamic pressure drop. Another optical emission study by Belakhovsky and Vorobjev (2016) showed that a nightside substorm occurred as a response to the SI^-. During the studied event, the pressure drop was accompanied by a further southward turning of the interplanetary magnetic field (IMF). This is consistent with the Liou (2007) results that more magnetic flux is needed for a substorm to occur.

There are many studies that investigate the magnetospheric and ionospheric sources of the two-step response (PI^+ and MI^+) during a solar wind dynamic pressure enhancement event. Most of these studies identify magnetospheric vortices as the source of MI^+ perturbation (Fujita et al., 2003b; Keller et al., 2002; Ozturk et al., 2017, 2018; Sibeck, 1990; Samsonov et al., 2010; Samsonov & Sibeck, 2013; Sun et al., 2014; Tian et al., 2016; Yu. & Ridley, 2011); however, the source of PI^+ perturbation is attributed to different mechanisms. Some of the proposed mechanisms are shock-intensified lobe reconnection (Samsonov et al., 2010), dusk to dawn electric fields at the magnetopause (Yu. & Ridley, 2011), transverse waves excited by the fast magnetosonic waves (Araki, 1994a; Tamao, 1965), localized solar wind impulses (Kataoka et al., 2004), and magnetospheric vortices (Kivelson & Southwood, 1991). However, another study conducted by Samsonov et al. (2006) showed that an interplanetary shock propagation can generate various different responses like slow expansion waves, contact discontinuities, and slow reversed shocks, depending on the magnetospheric conditions at the time of the shock passage. They concluded that the identification of these perturbations through measurements would be difficult due to the similarity in their propagation velocities.

The generation mechanisms of the two-step response to SI^- events are thought to be the mirror image of the SI^+ events (Fujita et al., 2004; Takeuchi et al., 2002; Zhang et al., 2010), but most of the aforementioned magnetospheric expansion studies relied on scarce observational data. One important modeling work on SI^-s was conducted by Fujita et al. (2004). Their simulation results confirmed that similar to the SI^+, oppositely directed FAC pairs form as a result of magnetospheric expansion, namely, during the PI^- and MI^- phases. Revisiting this study, Fujita et al. (2012) found out that both PI^- and MI^- FACs were associated with oppositely rotating magnetospheric vortices, followed by a third magnetospheric vortex system that was not previously reported during the SI^+s, indicating that the generation mechanisms of magnetospheric perturbations can differ. Fujita et al. (2012) was the first to link both FAC perturbations to magnetospheric vortices. More recently, Zhao et al. (2016) used equivalent ionospheric currents deduced from ground magnetometer observations and Time History of Events and Macroscale Interactions during Substorms (THEMIS) observa-
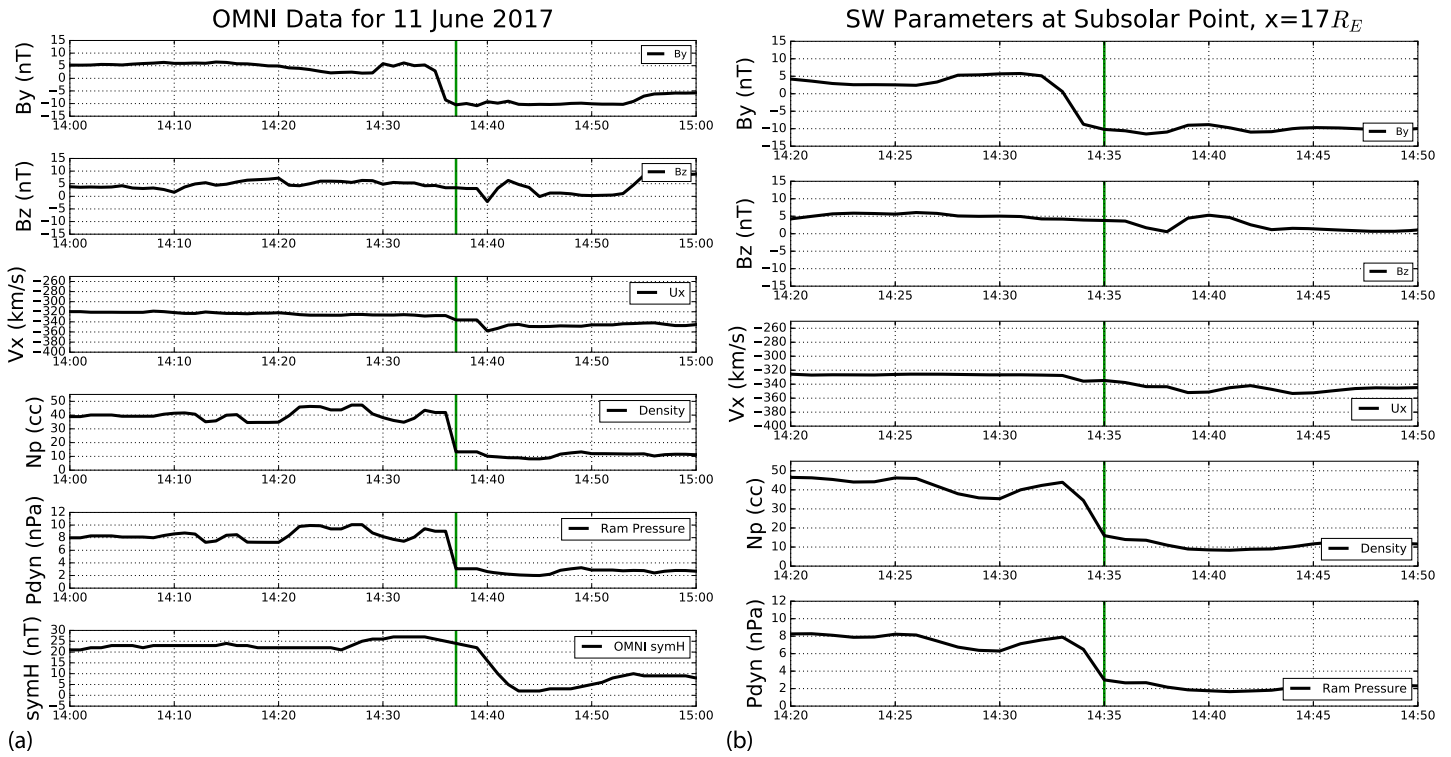
Figure 1. The IMF B_Y, B_Z, solar wind V_X, N_P, P_{dyn}, and *sym-H* values from OMNI solar wind database for the time interval between 1400 and 1500 UT (a) and the same parameters (except *sym-H*) extracted from the simulations at the subsolar point [17 R_E] for the time interval between 1420 and 1450 UT (b) are shown. The solid green line shows the time of the pressure drop.

tions together with a magnetohydrodynamic (MHD) simulation and identified the magnetospheric source region of observed ionospheric vortices. Their results showed a counterclockwise rotating vortex in the dawn sector in the equatorial magnetosphere during the MI^- phase as a result of the magnetospheric expansion.

In this paper, a sudden solar wind dynamic pressure decrease is investigated using global MHD and ionosphere-thermosphere (I-T) models as well as in situ spacecraft and ground magnetometer observations. The purpose of this study is to investigate the magnetospheric and ionospheric sources for the PI^- and MI^- signatures, determine the polarity distribution of the ground magnetometer responses to SI^-s, identify the ionospheric regions which are most prone to SI^- events, and understand how the ionosphere and thermosphere systems are affected in those regions.

2. Methodology

2.1. Simulation Setup

The 11 June 2017 1430–1500 UT interval was chosen to study the effects of the sudden solar wind dynamic pressure decreases on the geospace system. The Global Magnetosphere (GM), Inner Magnetosphere (IM), and Ionospheric Electrodynamics (IE) modules of the Space Weather Modeling Framework (Toth et al., 2005) were coupled to represent the magnetosphere system. The GM module, that is, University of Michigan Block Adaptive Tree Solarwind Roe Upwind Scheme (BATS-R-US), is used to solve for ideal MHD equations in GM domain and is two-way coupled with the Rice Convection Model (RCM; Toffoletto et al., 2003) that models the inner magnetosphere kinetic physics. Taking the time-dependent magnetic and electric field input from the GM module, RCM calculates the $E \times B$ and gradient curvature drifts to solve the particle transport equations. The GM module then transfers the field-aligned currents including the IM region to the high-latitude electrodynamics model. The Ridley Ionosphere Model (RIM) was used (Ridley et al., 2004) as the IE model. When coupled with global and inner magnetosphere models, it takes the Region 1 and Region 2 currents at the top of the ionosphere, generates a conductance pattern based on an empirical relation, and calculates the electric field potentials, which are then passed back to the GM module.
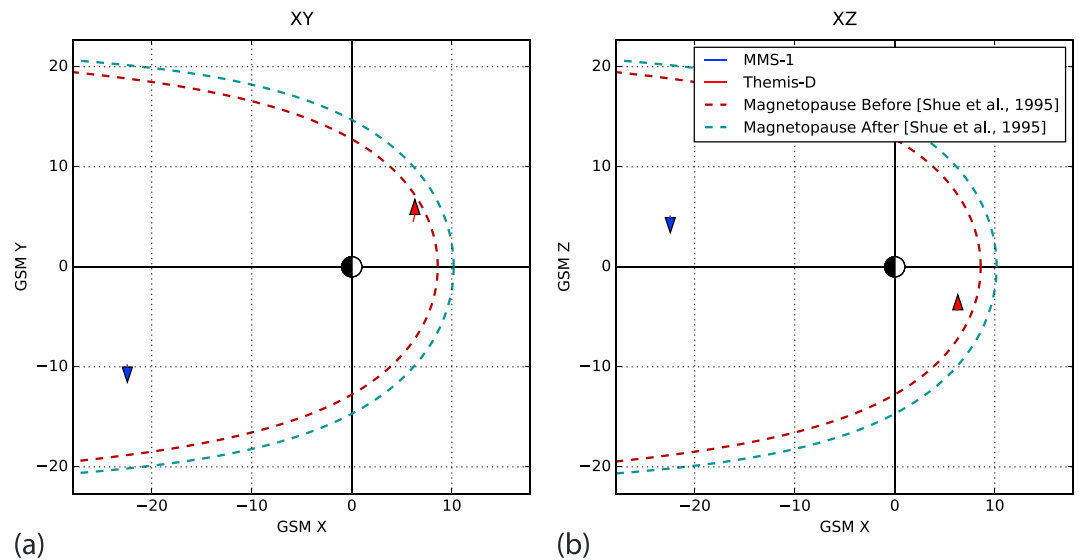
Figure 2. The positions of the MMS-1 (blue arrow) and THEMIS-D (red arrow) spacecraft are shown in GSM *XY* (a) and *XZ* (b) coordinates between 1430 and 1500 UT. The magenta dashed lines show the magnetopause boundary calculated with the Shue model, based on the interplanetary magnetic field and solar wind values before the dynamic pressure drop. The teal dashed lines show the magnetopause boundary after the dynamic pressure drop. GSM = geocentric solar magnetospheric; MMS = Magnetospheric Multiscale; THEMIS = Time History of Events and Macroscale Interactions during Substorms.

For this case study, the GM inner boundary is set to 2.5 R_E from the center of the Earth. The computational domain is a three-dimensional box in geocentric solar magnetospheric (GSM) coordinates that starts from 32 R_E upstream of the Earth in the X direction to 224 R_E tailward and $-128\,R_E$ to $+128\,R_E$ in both the Y and Z directions. The finest resolution is 1/8 R_E grid close to the Earth. Six hundred virtual ground magnetometers are implemented in both hemispheres uniformly from the magnetic equator up to 80° latitude (4° in latitude by 12° in longitude). The solar wind and IMF data from the OMNI Database are used to drive the model, which were propagated to the bow shock nose and are shown in Figure 1a.

Since the drivers for the simulation are taken from the OMNI Database, the simulation times are shifted back by 7 min, which is roughly the time for the solar wind to propagate from 32 R_E, the outer boundary of the simulation domain, to the Earth bow shock nose with the solar wind speed. Figure 1b shows the IMF and solar wind parameters extracted at the subsolar point, $x = 17R_E$ from the simulation. The green line shows the arrival of the solar wind dynamic pressure drop that impacted the Earth a couple of minutes later. The IMF B_Y was positive before the event, around 5 nT, but turned negative at 1438 UT and stayed around -10 nT during the event. The IMF B_Z was northward and did not show any strong variations during the interval. The change in solar wind velocity was small, around 20 km/s, during the event with no significant variations, but the solar wind density dropped from 42 to 10 cm^{-3}. Therefore, the solar wind dynamic pressure dropped from around 8 to 2 nPa. As the magnetosphere expanded, the outward motion of the magnetopause led to a reduction of the dawn-to-dusk magnetopause current. Consequently, the *sym-H* index dropped from 25 to 0 nT due to this dynamic pressure decrease.

The Global Ionosphere Thermosphere Model (GITM) simulations were driven with the OMNI solar wind data before the event, from 9 June 2017 at 1400 UT to 11 June 2017 at 1400 UT. The Weimer (2005) empirical model was used for the convection potential, while the OVATION Aurora Model (Newell et al., 2002) was used for particle precipitation during this interval. The particle precipitation and electric field solutions obtained from the global MHD model were then used to drive the GITM simulations starting from 11 June 2017 at 1400 to 1500 UT, updating the electrodynamic patterns every 10 s. The GITM simulations were run with a spatial resolution of 4° in longitude and 1° in latitude and an altitude range between 100 and 600 km.

2.2. Spacecraft Positions
Both THEMIS-D and Magnetospheric Multiscale (MMS) measured perturbations associated with the pressure change. The locations of the THEMIS-D and MMS-1 spacecraft are shown in Figure 2. THEMIS-D
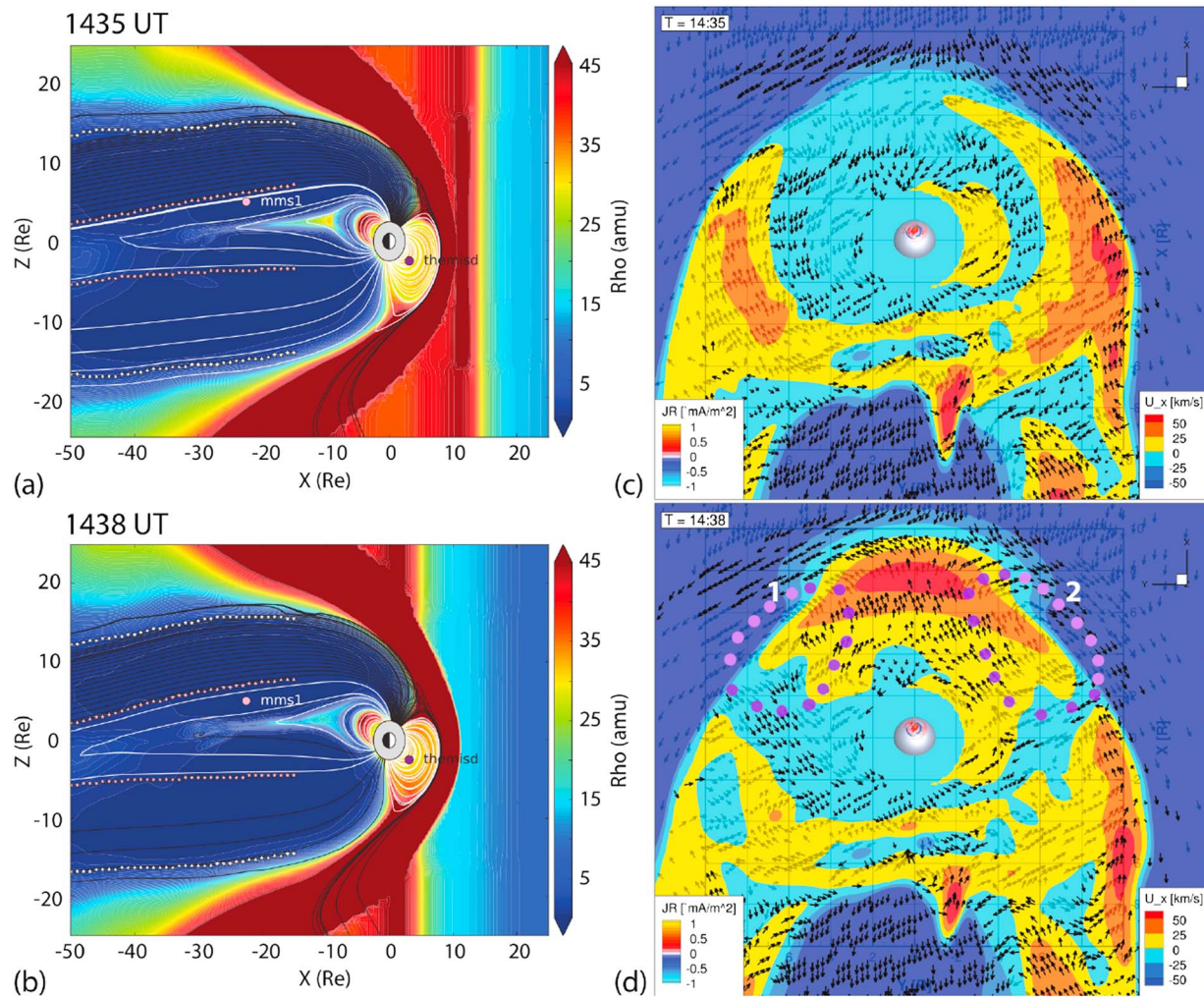
Figure 3. The pressure contours in the *XZ* plane with open (black) and closed (white) magnetic field lines are shown on the left for 1435 UT (a) and 1438 UT (b). The purple dot shows the location of THEMIS-D, whereas the pink dot shows the location of MMS-1. On the right, contours of V_X are plotted with magnetospheric flow vectors (c, d). The blue (red) contours on the top of the Northern Hemisphere show the magnetic field lines centered at the flow vortices that carry downward (upward) field-aligned currents at 1438 UT. Numbers 1 and 2 show the magnetospheric flow perturbations at the negative preliminary impulse phase. Purple dots indicate the locations of the flow perturbations associated with vortices 1 and 2. MMS = Magnetospheric Multiscale; THEMIS = Time History of Events and Macroscale Interactions during Substorms.

was located in the dayside afternoon sector [3.4, 10.7, −2.1 R_E], very close to the magnetopause before the decompression, while MMS-1 was located in the tail dawn sector [−22.4, −9.9, 5 R_E] during the event. The Electrostatic Analyzer (ESA) from THEMIS-D was used to understand the magnetospheric flows at this location, whereas the Fluxgate Magnetometer (FGM) from MMS-1 was used to understand the change in magnetic field configuration.

3. Results

3.1. Magnetospheric Response

Figures 3 and 4 show the evolution of the global magnetosphere system before and during the decompression. The temporal variation of the pressure profile in the *XZ* plane is shown in Figures 3a and 3b, including the locations of the MMS-1 and THEMIS-D spacecraft. The white dots show the location of the magnetopause lobe boundary, and the pink dots close to the $Z = 0$ plane mark the current sheet boundary. The front of the dynamic pressure drop can be seen as the red to blue transition propagating near 13 R_E at 1435 UT and 5 R_E at 1438 UT. The equatorial flow profile can be seen on the right (Figures 3c and 3d) with the solar wind and magnetosheath flow vectors. The contour colors represent the x component of the flow veloc-
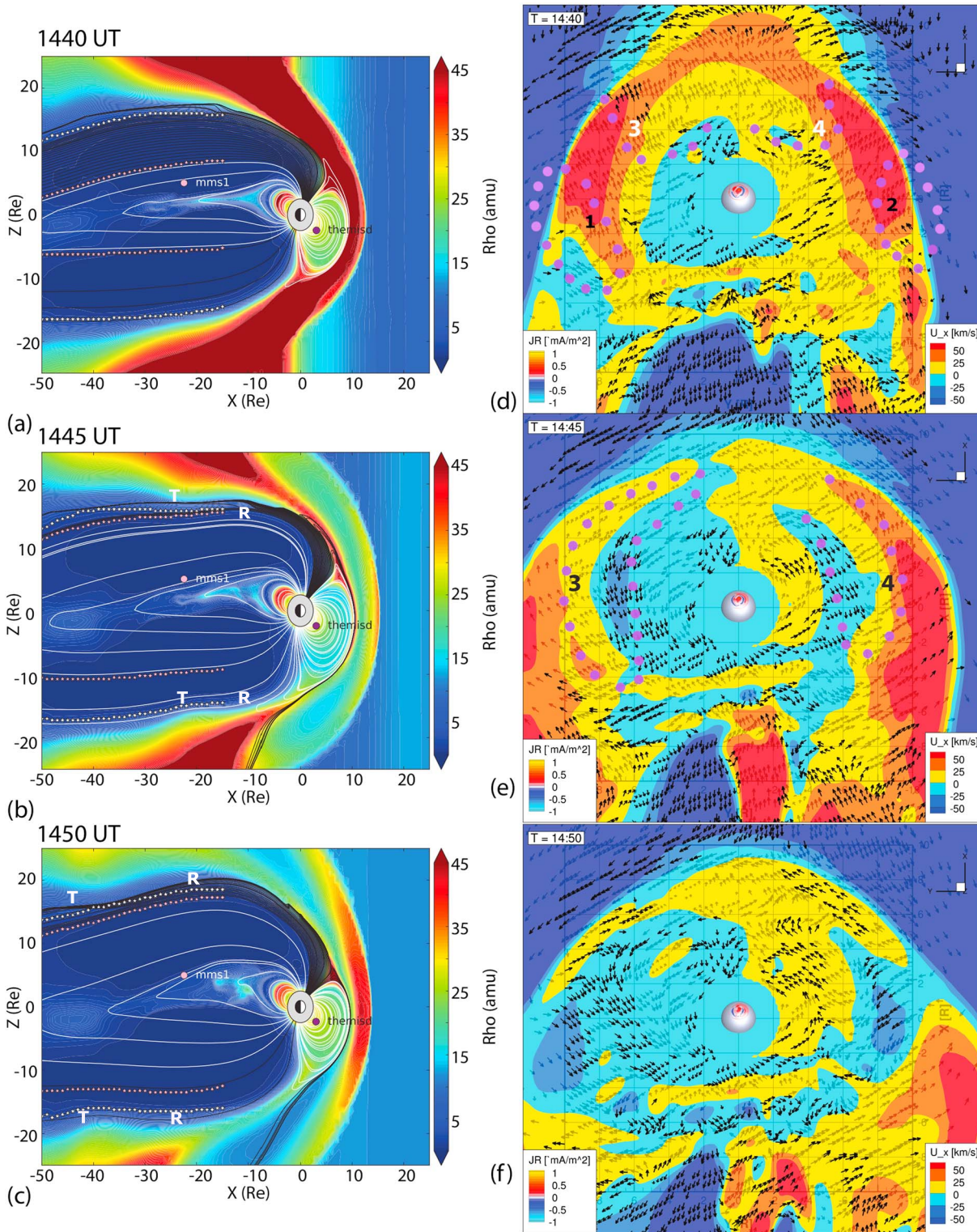
Figure 4. The pressure contours in the *XZ* plane with open (black) and closed (white) magnetic field lines are shown on the left for 1440 (a), 1445 (b), and 1450 UT (c). The purple dot shows the location of THEMIS-D, whereas the pink dot shows the location of MMS-1. On the right, contours of V_X are plotted with magnetospheric flow vectors (d–f). The blue (red) contours on the top of the Northern Hemisphere show the magnetic field lines centered at the flow vortices that carry downward (upward) field-aligned currents at 1440 UT. Numbers 3 and 4 show the magnetospheric flow perturbations at the negative main impulse phase. Purple dots indicate the locations of the flow perturbations associated with vortices 1, 2, 3, and 4. The T shows the wave through and the R shows the wave ridge. MMS = Magnetospheric Multiscale; THEMIS = Time History of Events and Macroscale Interactions during Substorms.
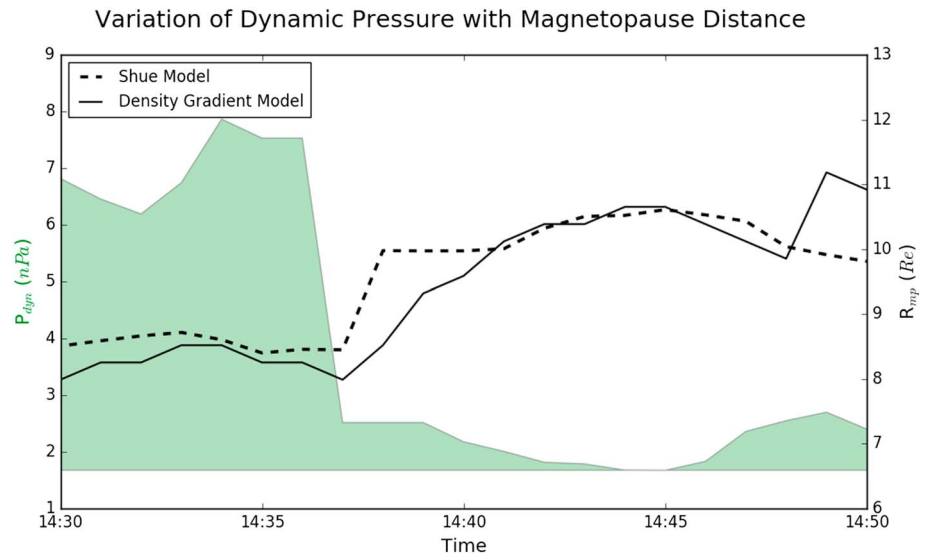
Figure 5. The variation of the magnetopause distance calculated with the Shue model (dashed) and density gradient (solid) with the solar wind dynamic pressure (green shading) in between 1430 and 1450 UT are shown.

ity. There were two channels of sunward flows located around $X = 2R_E, Y = 7R_E$, and $X = 6R_E, Y = -6R_E$ just before the decompression.

At 1438 UT, shown in Figures 3b and 3d, the nose of the magnetopause started to expand sunward. This resulted in two partial flow vortices at the dayside magnetosphere, one having a counterclockwise (CCW) sense of rotation in the dusk sector (marked with number 1) and the other having a clockwise (CW) sense of rotation in the dawn sector (marked with number 2). These vortices will be referred to as PI^- vortices from here on. There were also significant sunward flows at the nose of the subsolar magnetopause. Figures 4a and 4d show the magnetospheric response at 1440 UT when the low-density region in the solar wind propagated to $X = -2R_E$. The expansion of the magnetosphere in the downstream, shown in the XZ plane in Figures 4b and 4c, caused significant perturbations in the magnetotail. Near the location of the MMS-1 spacecraft, the magnetotail was no longer as highly stretched as it was during the compressed state, leading to a decrease in the B_X and an increase in the B_Z components, becoming more dipolarized. In the equatorial plane, shown in Figures 4e and 4f, a new pair of flow vortices emerged with opposite senses of rotation to the PI^- vortex at dusk (marked as 3) and dawn (marked as 4). Both pairs of vortices emerged inside the dayside magnetopause and propagated toward the nightside, eventually dissipating around 1450 UT (Figures 4c and 4f). These vortices will be referred to as MI^- vortices from here on. This outward motion and flow perturbations occurred close to the THEMIS-D spacecraft location.

The evolution of the magnetopause location at the subsolar point was also investigated during this time interval as shown in Figure 5. The magnetopause location was calculated using the Shue model driven by the OMNI data, as well as the MHD simulated magnetopause location calculated using the density gradient method described in Garcia and Hughes (2007). At 1437 UT, the dynamic pressure dropped from 7.5 to 2.4 nPa. The Shue model showed that the magnetopause location should have increased from $8.5R_E$ to $10R_E$, while the simulation results showed an expansion from $8R_E$ to $10R_E$, in agreement with the Shue model results.

Figure 6 shows the THEMIS-D ESA (a) and MMS-1 FGM (c) observations (blue) compared with the simulated satellite measurements (red). THEMIS-D initially recorded tailward flows in the dusk sector; however, as the magnetosphere started to expand, the flows became sunward and then fluctuated around 0. The V_Y component was initially positive in both the simulations and the observations followed by fluctuations around 0. The simulated V_X and V_Y flow components agreed with the observations qualitatively. These results indicate that a series of flow perturbations were recorded in the dusk sector first with a sense of counterclockwise and then with a sense of clockwise rotation. Figure 6b shows the velocity hodograms of THEMIS-D measurements and Space Weather Modeling Framework results between 1430 and 1445 UT. Both simulations and observations show a counterclockwise rotation followed by a clockwise rotation, sim-
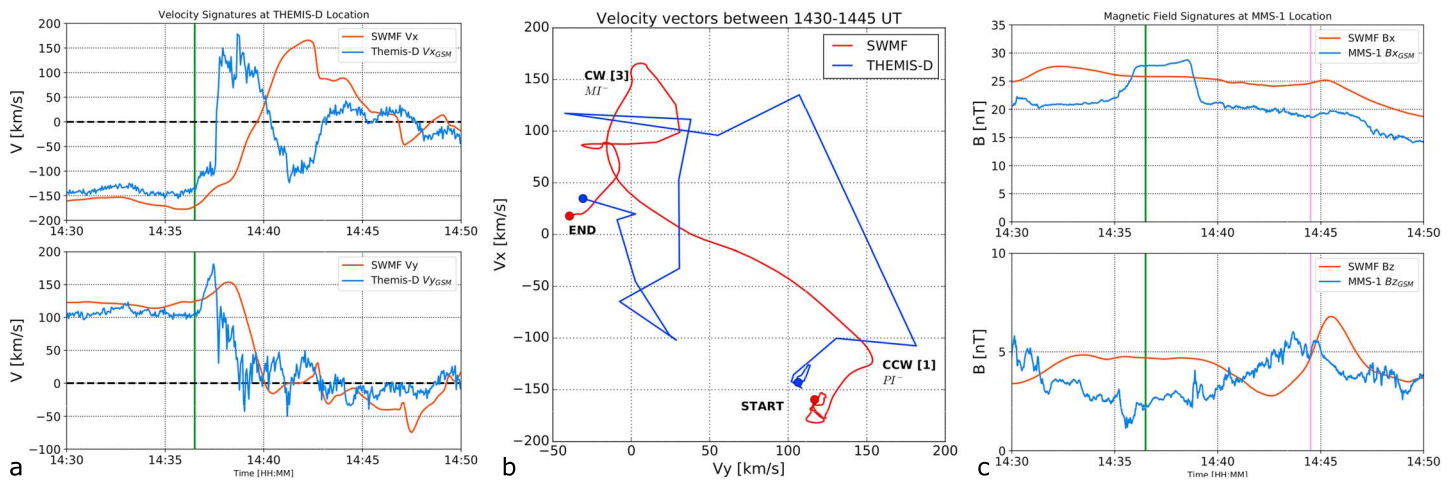
Figure 6. The comparison of satellite measurements (blue) with simulated satellite responses (red) for (a) velocity measurements (Vx on top, Vy on bottom) from THEMIS-D ESA and (c) magnetic field measurements (Bx on top, Bz on bottom) from MMS-1 FGM are shown between 1430 and 1450 UT. (b) The velocity hodogram constructed using THEMIS-D ESA data (blue) and simulation results (red) show a counterclockwise (ccw) and a clockwise (cw) rotation. The green shaded region for velocity measurements (a) marks the PI^- vortex, whereas the pink shaded region marks the MI^- vortex. The solid green line marks the arrival of the sudden dynamic pressure drop to the subsolar point at 1436 UT, and the solid pink line shows the arrival of the decompression front to the MMS-1 location at around 1445 UT (c). MMS = Magnetospheric Multiscale; SWMF = Space Weather Modeling Framework; THEMIS = Time History of Events and Macroscale Interactions during Substorms.

ilar to the magnetospheric flow perturbations marked with 1 and 3 in Figures 3 and 4. The vortex calculated from the THEMIS-D hodogram shows that the PI^- vortex was around $2.6R_E$ in X and $2R_E$ in Y, followed by the MI^- vortex which was around $6R_E$ in X and $6R_E$ in the Y directions.

The MMS-1 FGM measurements presented in Figure 6c show the effects of the sudden pressure decrease front propagation to the tail. As a result of the decreased pressure, the magnetopause flaring angle increased, as indicated by a B_X decrease, and a B_Z increase as observed in the MMS-1 measurements, at 1445 UT. The time of arrival with the drop of B_X and enhancement of B_Z was captured by the simulation.

3.2. Ionospheric Response

The evolution of the FACs, perturbation FACs, the Joule heating (MHD definition $\Sigma_p E^2$, first term in equation (5) of Thayer et al., 1995), and the horizontal magnetic perturbation profiles at the ground level were investigated to understand the ionospheric responses to the magnetospheric expansion. These maps are shown in Figure 7 at the same time cadences as the magnetospheric snapshots shown in Figures 3 and 4. Due to the IMF B_Z being northward, the FAC profile resembled the Northward Bz (NBZ) current system closely before the magnetospheric expansion. The Joule heating and magnetometer profiles at 1435 UT were chosen as the background conditions, and the values were subtracted from the following snapshots to highlight the effects of perturbation FACs. Figure 7b shows the responses 1 min after the expansion started. The perturbation FAC systems, which were obtained by subtracting the FAC profile from the previous minute, clearly showed an upward FAC at dusk (1) and a downward FAC at dawn (2). The polarities of these FACs were consistent with the rotational sense of the magnetospheric flow vortices in Figure 3 marked with 1 and 2. The Joule heating maps shown in the third row of Figure 7b increased slightly in between the perturbation FACs and decreased in the surrounding region. The magnetic field perturbations at the ground, shown in the fourth row of Figure 7b, indicated a positive perturbation (orange contours) at low latitudes between 3 and 19 MLT and in the high-latitude midnight sector. At the same time, the high-latitude magnetic perturbation response near dawn was negative.

Figure 7c shows the perturbed profiles at 1440 UT. At this time, a new pair of perturbation FACs appeared with opposite polarities as the PI^- FACs. These MI^- FACs were upward in the dawn (4) and downward (3) in the dusk sectors. The PI^- FACs (1, 2) had moved antisunward during this time. The Joule heating profile in the third row had increased clearly in the region between FACs 1–3 and 2–4, while weakened at the high latitudes. The ground magnetic perturbations also showed a clear dawn-dusk asymmetry in this instance, with a positive perturbation around 70° and between 4 and 11 MLT but negative elsewhere. Combining
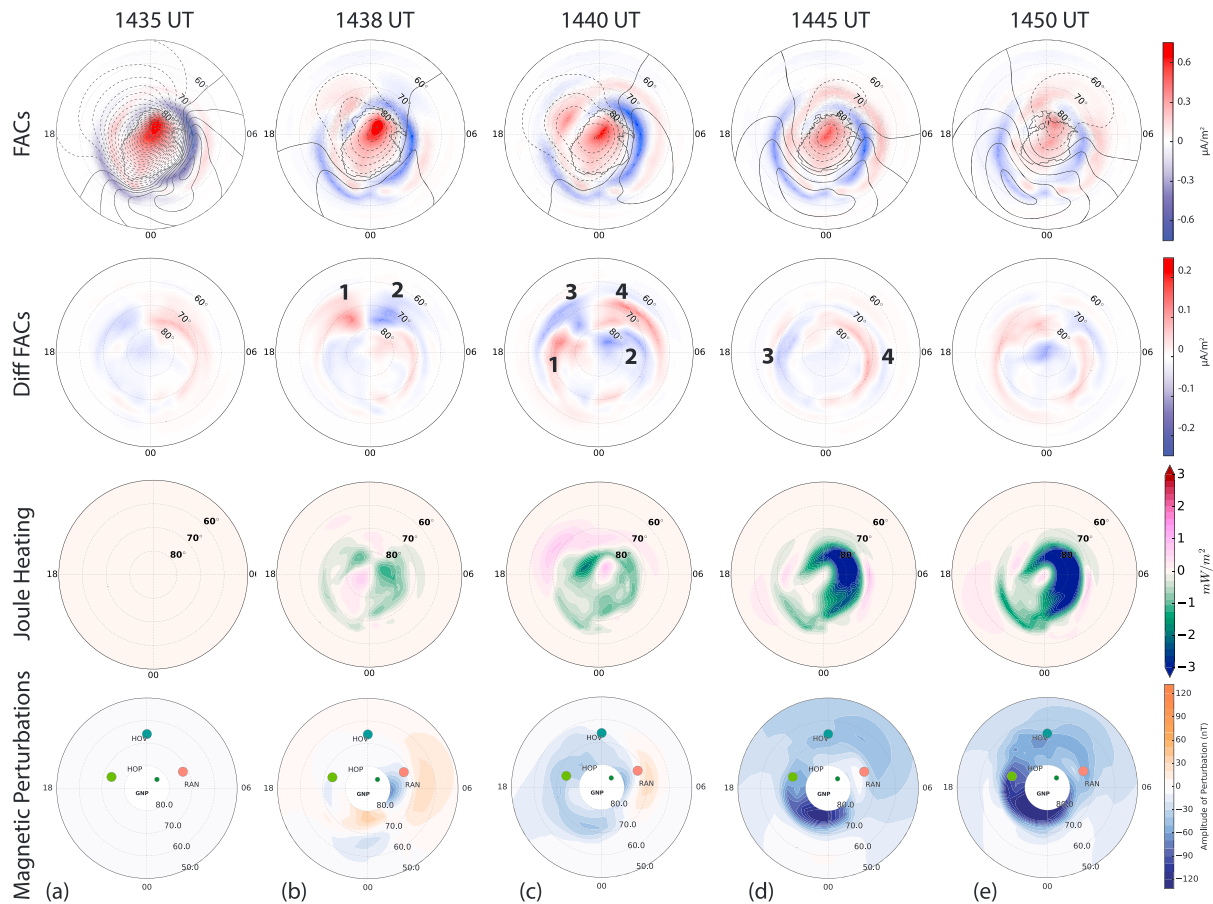
Figure 7. The FACs, perturbation FACs, Joule heating profile, and the simulated ground magnetometer responses to the solar wind dynamic pressure drop are shown for 1435 (a), 1438 (b), 1440 (c), 1445 (d), and 1450 UT (e). The numbers (1, 2, 3, and 4) show the perturbation FACs corresponding to magnetospheric flow perturbations. The green, blue, and pink dots in the bottom panels show the locations of the HOP, HOV, and RAN magnetometers. FAC = field-aligned current; HOP = Hopen Island magnetometer; HOV = Faroe Island magnetometer; RAN = Rankin Inlet magnetometer.

Figures 7b and 7c, it can be seen that the positive perturbations at the lower latitudes were short lived, similar to the observations shown in Araki and Nagano (1988).

At 1445 UT, the FAC profile started to recover from the pressure induced perturbations, as shown in Figure 7d. The electric field potentials and convection patterns changed significantly due to the sign change of the IMF B_Y. The Joule heating became slightly stronger in the dusk sector but decreased significantly at the dawn. The ground magnetic perturbations were strongly negative with the exception of the high-latitude region (> 70°) located between 5 and 10 MLT. The negative perturbation peaked near the high-latitude midnight sector.

At 1450 UT, the dayside FAC profile did not show significant perturbations; however, the electric field potentials in the nightside, especially in the dusk region, were denser. The transient currents showed another pair of FACs with an opposite sense to the MI^- FACs. These FACs were likely to be ULF wave harmonics (Fujita et al., 2012; Shi et al., 2013). Similar to previous cadence, the global Joule heating rate significantly decreased (blue shaded regions), but the weaker enhanced heating regions (shown in pink) associated with the PI^- and MI^- FACs propagated toward the midnight sector. Overall, the ground magnetic perturbation profile continued decreasing following the trend at 1445 UT.

Measurements from three magnetometer stations were selected and compared with the simulated magnetometer measurements to evaluate the fidelity of the simulation results. The locations of these magnetometers are shown in the fourth row of Figure 7. The magnetometers were chosen to sample the magnetic perturbation near 70° MLAT at dawn, noon, and dusk. The comparison of the observations with the simulation results are shown in Figure 8. A 3-min high-pass filter was applied to both the simulation results
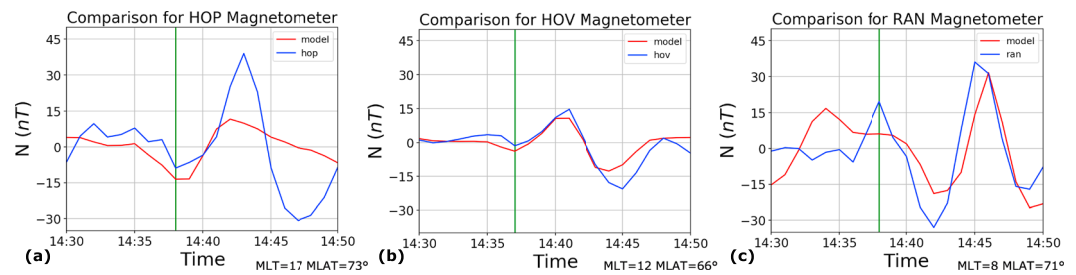
Figure 8. The comparison of the simulated north component of the magnetic field perturbations (red) with HOP (a), HOV (b), and RAN (c) magnetometer measurements (blue) are shown in between 1430 and 1500 UT. The solid green line shows the response to solar wind dynamic pressure drop. HOP = Hopen Island magnetometer; HOV = Faroe Island magnetometer; RAN = Rankin Inlet magnetometer.

and the magnetometer observations to subtract the response to the background activity. The Hopen Island (HOP) magnetometer, located in the dusk sector at the time, recorded an enhancement lasting 5 min, followed by a 4-min drop in the north (N) component of the magnetic field. The magnitude variation was not well captured by the simulated magnetometer. The drop in the simulated north component lasted longer in the simulated response. The Faroe Island (HOV) magnetometer recorded a slight 3-min enhancement followed by a larger 4-min drop in the magnetic field, which was captured by the model. This trend was opposite to the midlatitude magnetometer behavior reported in Ozturk et al. (2017) for local noon during SI^+s. The Rankin Inlet (RAN) magnetometer located in the dawn sector recorded a 4-min drop followed by a 4-min increase in the magnetic field. The responses of the HOV and RAN magnetometers to the magnetospheric expansion were well captured by the model; however, the simulation underestimated the magnitude of the perturbations, indicating the perturbations in the I-T system can be stronger than modeled. There was also a third response following the PI^- and MI^-, starting around 1448 UT at dawn and dusk sectors. This response was referred to as a second MI response by Fujita et al. (2005), but this recovery response is beyond
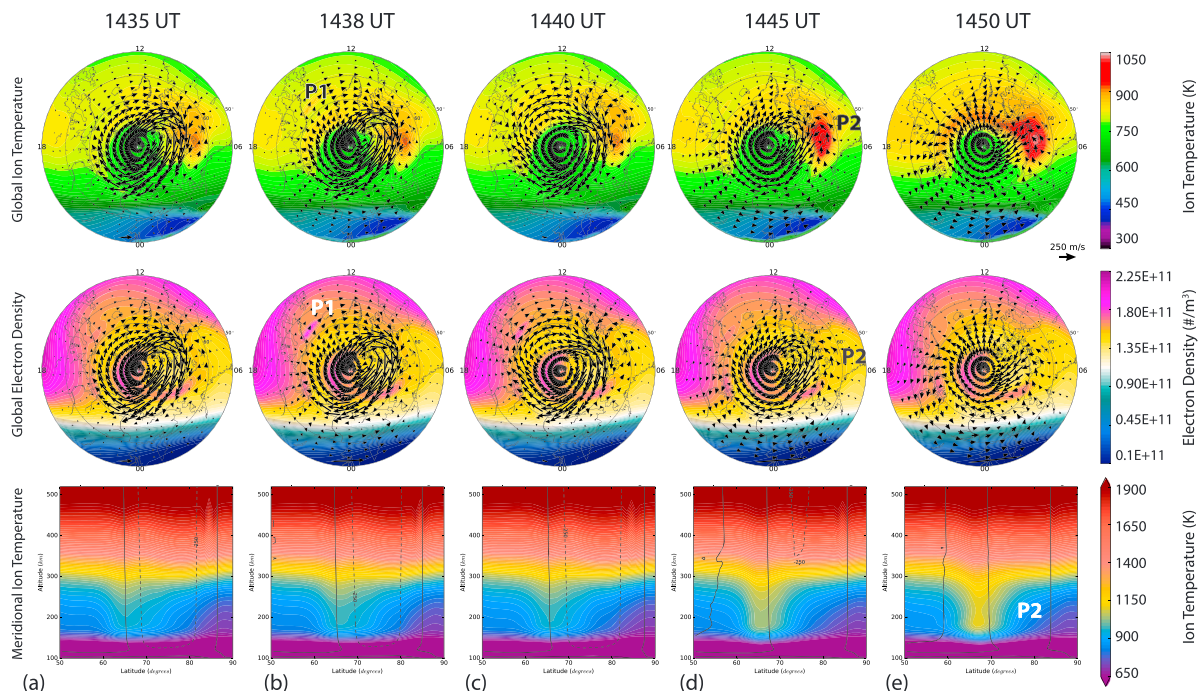

Figure 9. The Global Ionosphere Thermosphere Model results for ion temperature and convection profiles at 210 km (top row) and electron density (middle row) are shown for 1435 (a), 1438 (b), 1440 (c), 1445 (d), and 1450 UT (e). The bottom row shows the ion temperature for a meridional cut taken between 50° and 90° latitude at 11 LT, with horizontal ion convection velocities plotted on top for the same time steps. P1 and P2 show the location of ionospheric perturbations at 14.5 and 7.5 LTs, respectively.
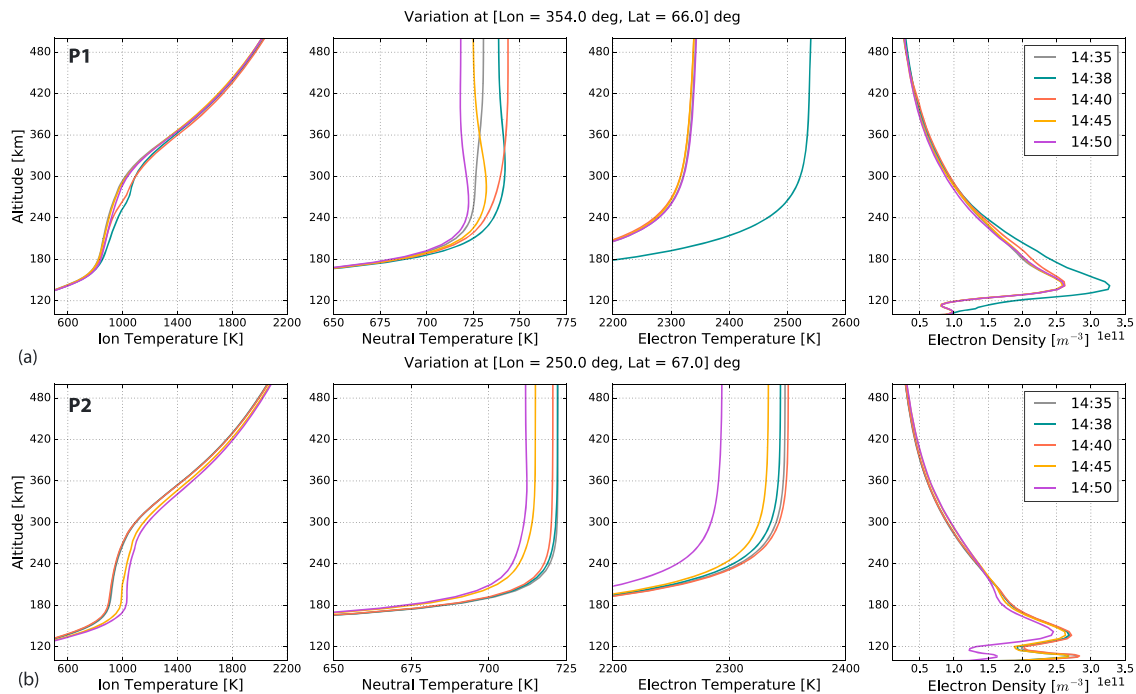
Figure 10. The altitude profiles (110–500 km) of ion, neutral, and electron temperature and electron density taken at 1435 (gray), 1438 (teal), 1440 (pink), 1445 (yellow), and 1450 UT (light green) for P1 [7.5 LT, 67°] (a) and for P2 [14.5 LT, 66°] (b) are shown.

the scope of this paper. Overall, the trend of the dawn and dusk magnetometers were opposite of the Araki Model (Araki, 1994a) for a dynamic pressure enhancement event.

Figure 9 shows the ion convection, temperature, and electron density variations from the GITM simulations, as a response to the sudden expansion of the magnetosphere. Figure 9a shows that the ion temperatures were below 1000 K everywhere before the event. The electron density at 210 km was depleted in regions with higher ion convection speeds, especially between 6 and 9 LT around 60° latitude. One minute after the start of the magnetospheric expansion, the ion temperature was enhanced over a very small area at 14.5 LT by around 50 K (P1) associated with the upward PI^- FACs. The ion convection direction between 15 and 19 LT, around 70° latitude changed from east to equatorward, whereas the convection velocities dropped in the region between 5 and 9 LT, around 60° latitude. At 1440 UT, the hot patch (P1) associated with the upward PI^- FACs disappeared. The ion convection flows that previously changed direction between 15 and 19 LT, around 70° latitude became eastward. The weakened eastward flows in the region between 5 and 9 LT, around 60° latitude, became poleward as shown in the top panel of Figure 9c. At 1445 UT, the region between 5 and 9 LT (P2) was significantly heated due to the directional change in IMF B_Y. The ion temperature further increased at 1450 UT in Figure 9e when the convection flows in the hot spot B were clearly westward moving against the prevailing neutral wind. In the bottom row, the meridional cut of ion temperature at 7.5 LT showed a hot ion channel formation at 67° latitude, which was the center of the hot spot P2.

Figure 10a shows the ion, neutral, electron temperature, and electron density profiles extracted from 66° latitude at the 14.5 LT, which corresponded to the perturbation shown as P1. The ion temperature profile change was small at this location, with the peak enhancement of 50 K occurring at 1438 UT between 240 and 300 km. The neutral temperature profile showed an enhancement by around 25 K between 1438 and 1440 UT, but the temperature dropped back to its initial values by 1445 UT. The electron temperature showed a significant increase of around 200 K at 1438 UT above 240 km due to the upward PI^- FAC, dropping back immediately afterward. In addition, the electron density below 240 km was enhanced by 20% at this location. One possible reason for the spontaneous enhancement of electron temperature and density are due to ionization and heating caused by the precipitating electrons (Schunk & Nagy, 2009) associated with the upward PI^- FACs over this location at 1438 UT.
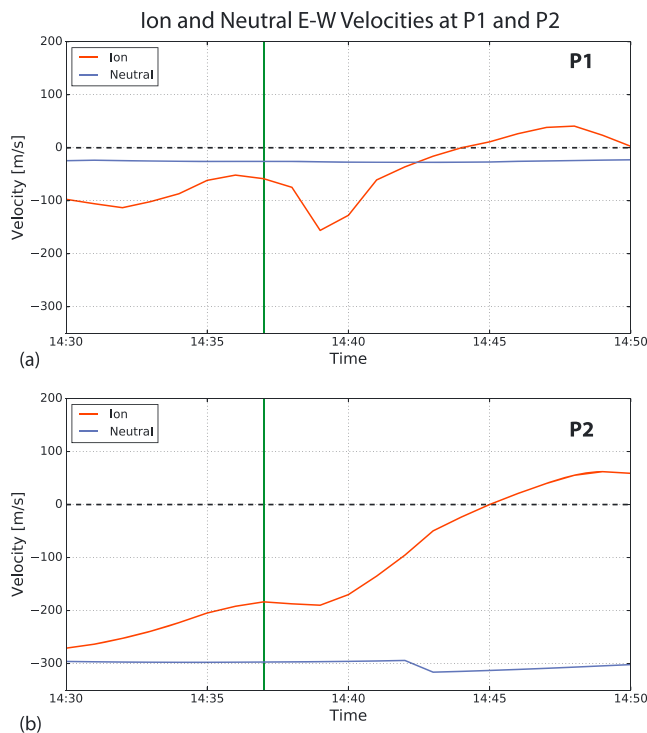
Figure 11. The simulated ion (red) and neutral (blue) E-W velocities extracted from 7.5 LT at 67° associated with the perturbation labeled as P1 (a) and 14.5 LT at 66° associated with the perturbation labeled as P2 (b) are shown.

Figure 10b shows the same profiles extracted from 67° latitude at the 7.5 LT, corresponding to the perturbation shown with P2 in 9. The simulation results showed that the ion temperature was enhanced by around 150 K at 1445 UT and by around 175 K at 1450 UT around 180 km. The neutral temperature showed an insignificant enhancement at 1445 UT, which was around 2 K. However, at 1450 UT the neutral temperature decreased by around 10 K above 240 km. The electron temperature dropped at this location as a response to magnetospheric expansion, with the largest change occurring at 1450 UT, which was around 100 K above 240 km. Similarly, the electron density decreased below 210 km with the most significant drop, 50%, occurring below 120 km at 1450 UT, due to the FACs moving away from P2.

Figure 11a shows the ion and neutral east-west (E-W) velocities extracted from the perturbation labeled as P1. Both the ion and neutral velocities were westward before the event. The ion velocities became increasingly westward during the PI^- phase but turned eastward during the MI^- phase. The peak difference occurred around 1438 UT, when ion convection vectors were enhanced further in the eastward direction due to the upward PI^- FAC. Figure 11b shows the same velocity profiles extracted from the location of the perturbation labeled as P2. Both the ion and neutral velocities were westward and significantly stronger than the velocities at P1. The ion velocity became increasingly eastward as the IMF B_Y changed sign. The reason for the large ion temperature increase seen at P2 in Figure 9 was this large difference between the ion and neutral velocities driving Joule heating.

4. Discussion and Conclusions

With the help of global and physics-based simulations, the response of the geospace system to a sudden solar wind dynamic pressure decrease event has been investigated. During the expansion of the magnetosphere, the simulated magnetospheric flows showed interesting features, especially during the PI^- phase. One of the most comprehensive studies investigating the magnetospheric response to SI^-s was conducted by Zhao et al. (2016). They reported THEMIS-A observations of a counterclockwise rotating vortex in the dawn sector and showed MHD simulation results of an oppositely rotating dawn-dusk vortex pair during the same time interval. The BATS-R-US MHD simulations reported above showed that immediately before the vortices reported in Zhao et al. (2016), another set of vortices, the PI^- vortices, existed in the magnetosphere and their presence was verified with THEMIS-D velocity observations in the dusk sector. Simulations reported in Fujita et al. (2004) also showed sunward flows in the dayside magnetosphere during the PI^- phase, but the partial vortex profile (Fujita et al., 2004) was not fully described, until the revisited study in Fujita et al. (2012). The source of the PI during dynamic pressure enhancements was associated with the magnetopause boundary (Fujita et al., 2003a; Kivelson & Southwood, 1991; Keller et al., 2002; Sibeck, 1990; Samsonov et al., 2010; Tian et al., 2016; Yu & Ridley, 2009); however, the proposed generation mechanisms differed. Samsonov et al. (2010) showed there are various different perturbations that can be generated during the compression of the magnetosphere. The propagation speed of these perturbations would depend on the magnetospheric conditions at the arrival time of the interplanetary shock. By employing an inner magnetospheric module, this study was able to demonstrate that magnetospheric return flows contribute to the vortex like flow perturbations in the magnetopause leading to the PI^- signatures. Furthermore, the measured ground magnetometer and simulated magnetic field responses in this study also indicated vortical structures through bipolar magnetic perturbation changes. The PI^- vortices were associated with an upward perturbation FAC in the dusk sector and a downward perturbation FAC in the dawn sector as shown in Figures 3 and 7. These FACs were responsible for the perturbations in the convection profiles which drove the Hall currents that caused a positive perturbation at dusk and a negative perturbation at dawn in the north component of the magnetic field.

The solar wind dynamic pressure dropped to a third of its previous value during the event reported in this study, which was lower than the 0.5 reported in Zhao et al. (2016) and 0.4 reported in Fujita et al. (2004).

The formation and propagation of the magnetospheric vortices depended on the propagation speed of the fast magnetosonic wave (Kivelson & Southwood, 1991; Sibeck, 1990). For the decompression event reported in this paper, the decompression front launched a fast magnetosonic wave through the magnetopause. A trough was formed due to the inward motion of the flank regions [$x = 6R_E$, $y = \pm 6R_E$], while the magnetopause nose radially expanded outward [$x = 8–10R_E, y = 0R_E$]. The magnetosphere continued expanding behind the solar wind discontinuity with a speed close to 90 km/s, until it reached to a pressure balance with the solar wind. The first set of magnetospheric vortices reported in this paper in association with the PI^- signatures formed as a result of the magnetopause boundary motion in which the boundary moved (i) inward, due to the propagation of the trough, (ii) sunward, due to the return flows in the magnetosphere, and (iii) outward, due to the propagation of the ridge, creating a counterclockwise rotating vortex at dusk and a clockwise rotating vortex at dawn. The second set of magnetospheric vortices in association with the MI^- signatures occurred as a result of (i) the outward motion due to the passage of the ridge and (ii) the sunward and (iii) the tailward flows due to the pressure gradients, forming a clockwise rotating vortex at dusk and a counterclockwise rotating vortex at dawn. The trough (T) and ridge (R) can be seen clearly in Figures 4b and 4c as the trough propagated from $x = -23R_E$ to $x = -40R_E$ in 5 min, whereas the trailing ridge amplitude grew. The generation mechanism for the magnetospheric vortices was attributed to the Kelvin-Helmholtz instability by Fujita et al. (2012).

The north component of the magnetic field perturbations on the ground, derived by virtual magnetometers, showed only slight deviations from the Araki model of SI^-s (Araki & Nagano, 1988). The perturbations associated with the PI^- phase between 1436 and 1440 UT showed an enhancement in the low-latitude dawn sector and high-latitude noon and midnight sectors. The MI^- phase perturbations from 1440 UT onward were mostly negative with strong dips in the low-latitude noon and high-latitude midnight sectors. One exception to the overall negative trend was seen at the high-latitude noon sector but with lower magnitudes than that of the negative dips. These differences from the Araki model can be attributed to various conditions such as solar EUV driven conductance patterns, which results in asymmetric distribution of the FACs between dayside and the nightside. Another reason can be the large and fluctuating IMF B_Y variations that introduce dawn-dusk asymmetries in the FAC profiles that in return determine the magnetic perturbations at the ground level. As this study showed, the superpositions of the magnetospheric perturbation flows and ionospheric perturbation currents on the preexisting profiles are extremely important in understanding the effects of such transients on the Magnetosphere-Ionosphere-Thermosphere system. Therefore, another reason for not observing an exact mirror image of SI^+ responses in the N component of magnetic field perturbations could be the conditions of the preexisting magnetosphere and ionosphere systems.

The ion convection flows and auroral signatures resulting from the sudden drop in the solar wind dynamic pressure altered the density and temperature profiles in the I-T system. These perturbations were further investigated using GITM with the electric field potentials and particle flux from MHD model. The Joule heating increased in a short-lived manner in regions sandwiched by the perturbation FACs, which results in an ion temperature increase by 50 K. Overall, the I-T system response to magnetospheric expansion showed a clear dawn-dusk asymmetry. The IMF B_Y changed sign during this event, causing the convection flows to change their direction from closely aligned with the neutral wind to its opposite direction. This direction change led to an increased frictional heating between ions and neutrals, causing the hot spot P2 seen in the morning sector, where the ion temperature increased by around 150 K.

This case study of the solar wind dynamic pressure decrease on 11 June 2017 revealed interesting magnetospheric flow profiles that were not evident in previous studies. Although this case was very useful in portraying the global response to a solar wind dynamic pressure decrease event, it also shows how helpful idealized simulations can be in understanding isolated effects of the solar wind drivers on the Magnetosphere-Ionosphere-Thermosphere system.

The geospace system response to the solar wind dynamic pressure decrease on 11 June 2017, between 1430 and 1500 UT, was studied using BATS-R-US and GITM simulations as well as in situ spacecraft and ground magnetometer observations. The electric field potential and particle precipitation profiles derived from the magnetospheric simulations were used to drive GITM. The main results of this study can be summarized as follows:

1. The dayside magnetosphere rapidly expanded sunward after the pressure decrease.
2. A pair of dawn-dusk vortices appeared at the dayside flanks as a response to magnetospheric expansion. These PI^- vortices had a counterclockwise sense of rotation at dusk and a clockwise sense of rotation at dawn.
3. Another pair of dawn-dusk vortices formed inside the magnetosphere following the PI^- vortices. These MI^- vortices had a clockwise sense of rotation at dusk and a counterclockwise sense of rotation at dawn.
4. These vortices mapped to the ionosphere as PI^- FACs (downward at dawn and upward at dusk) and MI^- FACs (upward at dawn and downward at dusk).
5. The peak Joule heating in the I-T system occurred between the perturbation FACs on the dayside driving an ion temperature increase by around 50 K in the afternoon sector. The IMF B_Y sign change in this case led to a change in the direction of the convection flow and an enhancement of 150 K in the ion temperature.
6. The polarity distribution of the magnetic field perturbations at the ground level slightly deviated from the SI^- model of Araki (1994a), which is a mirror image of the SI^+; however, this deviation is likely due to the variations in the IMF B_Y, but further idealized simulation studies are needed.

References

Araki, T. (1994a). Global structure of geomagnetic sudden commencement. *Planetary Space Science*, *25*, 373–384.

Araki, T. (1994b). A physical model of geomagnetic sudden commencement. In M. J. Engebreston, K. Takahashi, & M. Scholer (Eds.), *Solar wind sources of magnetospheric ultra-low-frequency waves* (Vol. 81, pp. 183–200). Washington, DC: American Geophysical Union.

Araki, T., & Nagano, H. (1988). Geomagnetic response to sudden expansion of the magnetosphere. *Journal of Geophysical Research*, *93*, 3983–3988.

Belakhovsky, V. B., & Vorobjev, V. G. (2016). Response of the night aurora to a negative sudden impulse. *Geomagnetism and Aeronomy*, *56*, 694–705.

Fujita, S., Tanaka, T., Kikuchi, T., Fujimoto, K., Hosokawa, K., & Itonaga, M. (2003a). A numerical simulation of the geomagnetic sudden commencement: 1. Generation of the field-aligned current associated with the preliminary impulse. *Journal of Geophysical Research*, *108*, 1416.

Fujita, S., Tanaka, T., Kikuchi, T., Fujimoto, K., & Itonaga, M. (2003b). A numerical simulation of the geomagnetic sudden commencement: 2. Plasma processes in the main impulse. *Journal of Geophysical Research*, *108*, 1417.

Fujita, S., Tanaka, T., Kikuchi, T., & Tsunomura, S. (2004). A numerical simulation of a negative sudden impulse. *Earth Planets Space*, *56*, 463–472.

Fujita, S., Tanaka, T., & Motoba, T. (2005). A numerical simulation of the geomagnetic sudden commencement: 3. A sudden commencement in the magnetosphere-ionosphere compound system. *Journal of Geophysical Research*, *110*, A11203. https://doi.org/10.1029/2005JA011055

Fujita, S., Yamagishi, H., Murata, K. T., Den, M., & Tanaka, T. (2012). A numerical simulation of a negative solar wind impulse: Revisited. *Journal of Geophysical Research*, *117*, A09219. https://doi.org/10.1029/2012JA017526

Garcia, K. S., & Hughes, W. J. (2007). Finding the Lyon-Fedder-Mobarry magnetopause: A statistical perspective. *Journal of Geophysical Research*, *112*, A06229. https://doi.org/10.1029/2006JA012039

Kataoka, R., Fukunishi, H., Fujita, S., Tanaka, T., & Itonaga, M. (2004). Transient response of the Earth's magnetosphere to a localized density pulse in the solar wind: Simulation of traveling convection vortices. *Journal of Geophysical Research*, *109*, A03204. https://doi.org/10.1029/2003JA010287

Keller, K. A., Hesse, M., Kuznetsova, M., Rastätter, L., Moretto, T., Gombosi, T. I., & DeZeeuw, D. L. (2002). Global MHD. Modeling of the impact of a solar wind pressure change. *Journal of Geophysical Research*, *107*(A7), 1126.

Kivelson, M. G., & Southwood, D. J. (1991). Ionospheric traveling convection vortex generation by solar wind buffeting of the magnetosphere. *Journal of Geophysical Research*, *96*, 1661–1667.

Liou, K. (2007). Large, abrupt pressure decreases as a substorm onset trigger. *Geophysical Research Letters*, *34*, L14107. https://doi.org/10.1029/2007GL029909

Newell, P. T., Sotirelis, T., Ruohoniemi, J. M., Carbary, J. F., Liou, K., Skura, J. P., et al. (2002). Ovation: Oval variation, assessment, tracking, intensity and online nowcasting. *Annales Geophysicae*, *20*, 1039–1047.

Ozturk, D. S., Zou, S., Ridley, A. J., & Slavin, J. A. (2018). Modeling study of the geospace system response to the solar wind dynamic pressure enhancement on 17 March 2015. *Journal of Geophysical Research: Space Physics*, *123*, 2974–2989. https://doi.org/10.1002/2017JA025099

Ozturk, D. S., Zou, S., & Slavin, J. A. (2017). IMF by effects on ground magnetometer response to increased solar wind dynamic pressure derived from global MHD simulations. *Journal of Geophysical Research: Space Physics*, *122*, 5028–5042. https://doi.org/10.1002/2017JA023903

Ridley, A. J., Gombosi, T. I., & DeZeeuw, D. L. (2004). Ionospheric control of the magnetosphere: Conductance. *Annales Geophysicae*, *22*, 567–584.

Samsonov, A. A., Němeček, Z., & Šafránková, J. (2006). Numerical MHD modeling of propagation of interplanetary shock through the magnetosheath. *Journal of Geophysical Research*, *111*, A08210. https://doi.org/10.1029/2005JA011537

Samsonov, A. A., & Sibeck, D. G. (2013). Large-scale flow vortices following a magnetospheric sudden impulse. *Journal of Geophysical Research: Space Physics*, *188*, 3055–3064. https://doi.org/10.1002/jgra.50329

Samsonov, A. A., Sibeck, D. G., & Yu, Y. (2010). Transient changes in magnetospheric-ionospheric currents caused by the passage of an interplanetary shock: Northward interplanetary magnetic field case. *Journal of Geophysical Research*, *115*, A05207. https://doi.org/10.1029/2009JA014751

Sato, N., Murata, Y., Yamagishi, H., Yukimatu, A. S., Kikuchi, M., Watanabe, M., et al. (2001). Enhancement of optical aurora triggered by the solar wind negative pressure impulse. *Geophysical Research Letters*, *28*(1), 127–130.

Schunk, R., & Nagy, A. (2009). *Ionospheres: Physics, plasma physics and chemistry*. Cambridge, UK: Cambridge University Press.

Shi, Q. Q., Hartinger, M. D., Angelopoulos, V., Tian, A. M., Fu, S. Y., Zong, Q.-G., et al. (2013). Solar wind pressure pulse-driven magnetospheric vortices and their global consequences. *Journal of Geophysical Research: Space Physics*, *119*, 4274–4280. https://doi.org/10.1002/2013JA019551

Sibeck, D. G. (1990). A model for the transient magnetospheric response to sudden solar wind dynamic pressure variations. *Journal of Geophysical Research*, *95*, 3755–3771.

Sun, T. R., Wang, C., Zhang, J. J., Pilipenko, V. A., Wang, Y., & Wang, J. Y. (2014). The chain response of the magnetospheric and ground magnetic field to interplanetary shocks. *Journal of Geophysical Research: Space Physics*, *120*, 157–165. https://doi.org/10.1002/2014JA020754

Takeuchi, T., Araki, T., Luehr, H., Rasmussen, O., Watermann, J., Milling, D. K., et al. (2000). Geomagnetic negative sudden impulse due to a magnetic cloud observed on May 13, 1995. *Journal of Geophysical Research*, *105*(A8), 18,835–18,846.

Takeuchi, T., Araki, T., Viljanen, A., & Watermann, J. (2002). Geomagnetic negative sudden impulses: Interplanetary causes and polarization distribution. *Journal of Geophysical Research*, *107*(A7), 1096.

Tamao, T. (1965). Transmission and coupling resonance of hydromagnetic disturbances in the non-uniform Earth's magnetosphere.

Thayer, J. P., Vickrey, J. F., Heelis, R. A., & Gary, J. B. (1995). Interpretation and modeling of high-latitude electromagnetic energy flux. *Journal of Geophysical Research*, *100*, 19,715–19,728.

Tian, A. M., Shen, X. C., Shi, Q. Q., Tang, B. B., Nowada, M., Zong, Q. G., & Fu, S. Y. (2016). Dayside magnetospheric and ionospheric responses to solar wind pressure increase: Multispacecraft and ground observations. *Journal of Geophysical Research: Space Physics*, *121*, 10,813–10,830. https://doi.org/10.1002/2016JA022459

Toffoletto, F., Sazykin, S., Spiro, R., & Wolf, R. (2003). Inner magnetospheric modeling with the Rice Convection Model. *Space Science Reviews*, *107*, 175–196.

Toth, G., Sokolov, I. V., Gombosi, T. I., Chesney, D. R., Clauer, C. R., DeZeeuw, D. L., et al. (2005). Space Weather Modeling Framework: A new tool for the space science community. *Journal of Geophysical Research*, *110*, A12226. https://doi.org/10.1029/2005JA011126

Weimer, D. R. (2005). Predicting surface geomagnetic variations using ionospheric electrodynamic models. *Journal of Geophysical Research*, *110*, A12307. https://doi.org/10.1029/2005JA011270

Yu, Y., & Ridley, A. J. (2009). The response of the magnetosphere-ionosphere system to a sudden dynamic pressure enhancement under southward IMF conditions. *Annales Geophysicae*, *27*, 4391–4407.

Yu., Y., & Ridley, A. J. (2011). Understanding the response of the ionosphere-magnetosphere system to sudden solar wind density increases. *Journal of Geophysical Research*, *116*, A04210. https://doi.org/10.1029/2010JA015871

Zhang, X. Y., Zong, Q. G., Wang, Y. F., Zhang, H., Xie, L., Fu, S. Y., et al. (2010). ULF waves excited by negative/positive solar wind dynamic pressure impulses at geosynchronous orbit. *Journal of Computational Physics*, *115*, A10221. https://doi.org/10.1029/2009JA015016

Zhao, H. Y., Shen, X. C., Tang, B. B., Tian, A. M., Shi, Q. Q., Weygand, J. M., et al. (2016). Magnetospheric vortices and their global effect after a solar wind dynamic pressure decrease. *Journal of Geophysical Research: Space Physics*, *121*, 1071–1077. https://doi.org/10.1002/2015JA021646

Zhou, X., & Tsuratani, B. T. (1999). Rapid intensification and propagation of the dayside aurora: Large scale interplanetary pressure pulses (fast shocks). *Geophysical Research Letters*, *26*, 1097–1100.